ACS APPLIED MATERIALS & INTERFACES

Research Article

www.acsami.org

Macroporous SnO_2 Synthesized via a Template-Assisted Reflux Process for Efficient Dye-Sensitized Solar Cells

Ke-Nan Li, Yu-Fen Wang, Yang-Fan Xu, Hong-Yan Chen, Cheng-Yong Su, and Dai-Bin Kuang*

MOE Key Laboratory of Bioinorganic and Synthetic Chemistry, KLGHEI of Environment and Energy Chemistry, State Key Laboratory of Optoelectronic Materials and Technologies, Lehn Institute of Functional Materials, School of Chemistry and Chemical Engineering, Sun Yat-sen University, Guangzhou 510275, P. R. China

ABSTRACT: Macroporous SnO_2 composed of small SnO_2 nanoparticles with diameters around 10 nm is prepared via a reflux process. This novel structure is designed as the photoanode in dye-sensitized solar cells (DSSCs), intending to improve the light utilization efficiency with its excellent light scattering ability. Though the dye adsorption of macroporous SnO_2 (14.00×10^{-8} mol cm^{-2}) is lower than that of SnO_2 nanoparticles (19.24×10^{-8} mol cm^{-2}), the photovoltaic performance of the DSSCs based on the former is 4.87% compared to 4.41% for SnO_2 nanoparticles, showing over 10% increment than the latter. This improvement is mainly due to the enhanced light scattering ability and charge collection efficiency of the macroporous structure, both of which contribute to a higher short current density and hence for the better power conversion efficiency. Furthermore, a double-layer structure composed of SnO_2 nanoparticles (active layer) and macroporous SnO_2 (scattering layer) possess both large dye adsorption (22.82×10^{-8} mol cm^{-2}) and scattering property, thus leads to a significant overall conversion efficiency of 5.78%.

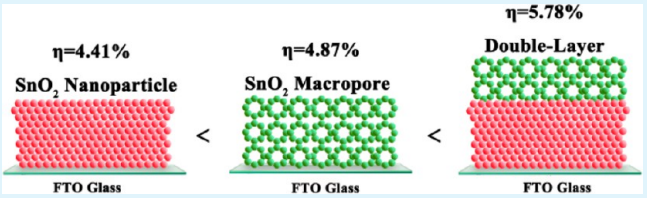

KEYWORDS: *dye-sensitized solar cells, macroporous SnO_2, reflux, light scattering, photovoltaic performance, polystyrene*

INTRODUCTION

Dye-sensitized solar cell (DSSC) is typically composed of metal-oxide semiconductor film coated fluorine-doped tin oxide (FTO) glass,[1−3] dye,[4,5] electrolyte,[6,7] and Pt counter electrode,[8] which has been attracting immense research interest since the great breakthrough made by Michael Grätzel in 1991.[9] So far, the photoelectrical conversion efficiency of 12.3%[10] has been reported through the optimization of photoelectrode, sensitizer, and electrolyte. As an important part of DSSCs, photoanode materials are related to the dye loading, light scattering, electron injection, transport and recombination, which largely influence the power conversion efficiency. Except the widely investigated TiO_2 photoanode,[11−16] some other metal-oxide semiconductors, such as tin dioxide (SnO_2),[17−20] zinc oxide (ZnO)[21−25] and zinc stannate (Zn_2SnO_4),[26−30] also received more and more attention. The performance of SnO_2 photoanodes was poorer than TiO_2 due to the faster interfacial electron recombination and lower trapping density of the former,[31] which led to a lower open-circuit voltage and fill factor. However, there are two advantageous characteristics of SnO_2 compared to TiO_2 attracting significant attention for DSSCs devices: i) it has higher electron mobility (100−200 cm^2 V^{-1} S^{1-})[32] than TiO_2 (0.1−1.0 cm^2 V^{-1} S^{1-}),[33] indicating a faster electrons diffusion transport in SnO_2; ii) it has a larger band gap (3.8 eV) than TiO_2 (anatase, 3.2 eV), thus reduces the oxidative holes created in the valence band,[34] which is able to give a long-term stability for DSSCs. Recently, various morphologies of SnO_2 have been synthesized and exhibited interesting photovoltaic performance in DSSC applications. For example, the SnO_2 nanorod, nanowire or nanotube have shown power conversion efficiencies of 1.5−5.6%.[35−37] Recently, more than 6% photovoltaic performance has been reported for the hierarchical SnO_2 octahedra photoanode.[17,18]

Macroporous structure is becoming more and more interesting in DSSCs because of its several advantages such as the ordered networks can offer fast electron transport paths, and ordered macropores can enhance light scattering, facilitate infiltration of the electrolyte solution, and promote mass transport, especially for the ionic liquid, gel or polymer based quasi- or solid state electrolyte with a high viscosity. According to literature, there have been several articles about macroporous and hollow SnO_2 structure based DSSCs, which have obtained conversion efficiencies over 5%.[38,39] The impressive performance compared to that of nanocrystals based DSSCs is mainly because of the highly optical electrode that can ensure better light harvesting efficiency, faster charge extraction and reduced interfacial recombination.[39]

Herein, we present a macroporous SnO_2 structure synthesized by a facile template-assisted reflux method. By using polystyrene (PS) microspheres of 750 nm as the template, a macroporous SnO_2 (macro-SnO_2) with pore diameter of 600 nm can be achieved, which is built up by SnO_2 nanoparticles of 10 nm in diameter. Meanwhile, in the absence of PS sphere, the products are SnO_2 nanoparticles

Received: March 17, 2013
Accepted: May 21, 2013
Published: May 21, 2013

   dx.doi.org/10.1021/am4009727 | ACS Appl. Mater. Interfaces 2013, 5, 5105−5111

($NP\text{-}SnO_2$) with the sizes about 10 nm. With better scattering ability and faster electron transport, the photovoltaic performance of DSSCs based on macro-SnO_2 photoelectrode shows an enhancement compared to that of NP-SnO_2. Finally, the double-layered photoanode (double-layer SnO_2) with SnO_2 nanoparticles as the bottom layer and macroporous SnO_2 top layer exhibits an excellent conversion efficiency of 5.78% under AM-1.5 G one sun light intensity. Such structure can both ensure the amount of dye adsorption and provide an increased path length of incident light in SnO_2 films for a better light utilization.

EXPERIMENTAL SECTION

Preparation of NP-SnO_2 and Macro-SnO_2. The monodisperse 750 nm polystyrene (PS) microspheres were used as template and synthesized in an emulsifier-free system.[40] The polymerization reaction was carried out in a 1000 mL round-bottom three-necked flask. Styrene and potassium persulphate were the main reactants and the whole reaction was under the temperature of 70 ± 1 °C. After 24 h of thermostatic with stirring and N_2 atmosphere, 750 nm PS lattices were obtained.

The macroporous SnO_2 was synthesized by hot reflux method at a constant temperature of 100 °C. Typically, a 250 mL round-bottom two-necked flask was needed, one outlet was for the water-cool condenser and the other was for a dropping funnel. Five mmol of $SnCl_2{\cdot}2H_2O$ power (A. R.) were dissolved in 50 mL of absolute ethanol and kept stirring for 30 min, forming a 0.1 M transparent solution, then the solution was slowly added to the flask containing 25 mL distilled H_2O and 25 mL of PS latices with vigorous stirring via the dropping funnel, the flask was settled in an oil bath of 100 °C that was beforehand prepared. This system was kept for 12 h with continual stirring and a temperature of 100 °C. The resultant reaction solution was centrifuged at 7000 rpm for 5 min after cooling to room temperature, then it was washed with distilled water and absolute ethanol by an ultrasonic cleaning bath. The precipitate was collected as resultant product after repeating the washing procedure 5 times, and was dried at 60 °C. After drying, the powers were calcined at 500 °C for 1 h to obtain the final products for further characterizations. In order to give comparative performance of different SnO_2 structures in DSSCs, SnO_2 nanoparticles were synthesized with this method as well, which just replaced the PS lattices with distilled water and kept the previous concentration of other reactants.

Preparation of SnO_2 Paste. Hierarchical macro-SnO_2 or NP-SnO_2 (1.0 g) were ground for 40 min in the mixtures of ethanol (8.0 mL), acetic acid (0.2 mL), terpineol (3.0 g), and ethyl cellulose (0.5 g) to form a slurry, and then the mixtures were sonicated for 5 min in an ultrasonic bath, finally to form a viscous white SnO_2 paste.

Assembly of NP-SnO_2 and Macro-SnO_2 DSSCs. A thin compact lay of SnO_2 sol–gel (~60 nm) was coated onto FTO glass (15 Ω/square, Nippon Sheet Glass, Japan) by spraying SnO_2-ethanol solution followed by calcinations at 500 °C, intending to prevent a direct contact between electrolyte and FTO glass. The SnO_2 colloidal (5 nm) solution was prepared from $SnCl_4$, acetylacetone, n-butanol and para-toluene-sulfonic acid by refluxing the mixture of them at 60 °C for 12 h. The NP and macroporous SnO_2 paste were screen printed onto as-prepared FTO glass and sintered at 500 °C. The after-sintered films were soaked in 0.04 M $TiCl_4$ aqueous solution for 30 min and heated at 520 °C for 30 min. Then the films were immersed in 0.05 mM N719 dye ($Ru[LL'\text{-}(NCS)_2]$, L = 2,2′-bipyridyl-4,4′-dicarboxylicacid, L = 2,2′-bipyridyl-4,4′-ditetrabutyllammonium carboxylate, Solaronix Co.). The films were taken out and sandwiched together with Pt counter electrode after 24 h sensitization. The Pt counter electrode was made by thermal decomposition of H_2PtCl_6 solution (5 mM in isopropanol) on FTO glass at 400 °C for 15 min. A solution containing I^-/I_3^- composed of 0.6 M 1-methyl-3-propylimidazo-lium iodide (PMII), 0.1 M guanidinium thiocyanate, 0.03 M I_2, 0.5 M tertbutylpyridine dissolved in acetonitrile, and valeronitrile (85:15) was prepared as liquid electrolyte, which was injected into cells.

Characterization of NP-SnO_2 and Macro-SnO_2. A X-ray diffraction (XRD, Bruker D8 Advance X-ray diffractometer with Cu Kα radiation, λ = 1.5418 Å) was used to examine the crystalline phase purity of powder samples. The morphologies, sizes, and intrinsic structures of the NP-SnO_2 and macro-SnO_2 were observed by field-emission scanning electron microscopy (FE-SEM, JSM-6330F), transmission electron microscopy (TEM, JEOL-2010 HR), high-resolution transmission electron microscope (HRTEM) and selected area electron diffraction (SAED). The active DSSC area was measured with a profilometer (Ambios, XP-1). To investigate their light absorption, scattering properties, a UV–vis–NIR spectrophotometer (UV-3150) was used. The dye adsorptive capacity was also investigated after desorption in 0.1 M NaOH solution via a UV–vis–NIR spectrophotometer (UV-3150). The Spectral Products DK240 monochromator was carried out to give an incident light from 380 to 800 nm for the IPCE measurement. The photocurrent density–voltage curves (J–V) were studied employing a Keithley 2400 source meter under one sun AM 1.5G (100 mW cm^{-2}) illumination with a solar light simulator (Oriel, model 91192). A NREL-calibrated Si cell with an optical filter was used to adjust the light intensity of a 1000 W xenon arc lamp (Oriel, model 6271) that served as the light source. Electrochemical impedance spectra (EIS) were measured applying a bias potential of −0.7 V in dark and a frequency range from 10 mHz to 1 MHz. The impedance parameters were obtained using a Z-view software. Intensity −modulated photovoltage spectroscopy (IMVS) and intensity-modulated photocurrent spectroscopy (IMPS) were measured with the electrochemical workstation (Zahner, Zennium) and a light source (Zahner, PP211).

RESULTS AND DISCUSSION

Both NP-SnO_2 and macro-SnO_2 were prepared by reflux reaction in the absence or presence of PS sphere, respectively. Figure 1 shows the XRD patterns of the two samples, and each

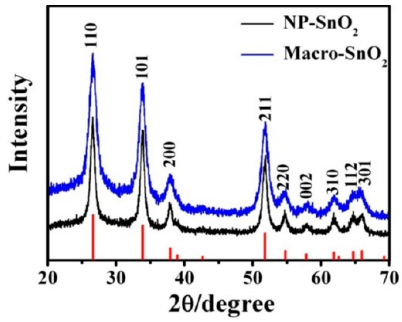

Figure 1. XRD patterns of as-synthesized SnO_2 nanoparticles and macroporous SnO_2.

peak is marked corresponding to the crystal plane index, indicating their tetragonal phase of SnO_2 (JCPDS 41–1445). No other miscellaneous peaks can be observed implying the high crystal purity.

The surface morphologies of PS and macroporous SnO_2 were characterized by Field emission scanning electron microscopic (FE-SEM) and shown in Figure 2. FE-SEM result indicates (Figure 2a) that the PS microsphere has uniform size of 750 ± 10 nm. In the absence of PS sphere, the sample prepared via reflux and a followed calcination process (500 °C for 1 h) is SnO_2 nanoparticles with size of ~10 nm (Figure 2b). When using the 750 nm PS sphere template (Figure 2c), the macroporous SnO_2 structure with an imperfect ordered array possessing a pore diameter about 600 nm is observed. The reduction of ~150 nm for the pore size compared to the original PS microsphere template is mainly ascribed to the contraction of structure during the calcination procedure. It is

dx.doi.org/10.1021/am4009727 | ACS Appl. Mater. Interfaces 2013, 5, 5105–5111

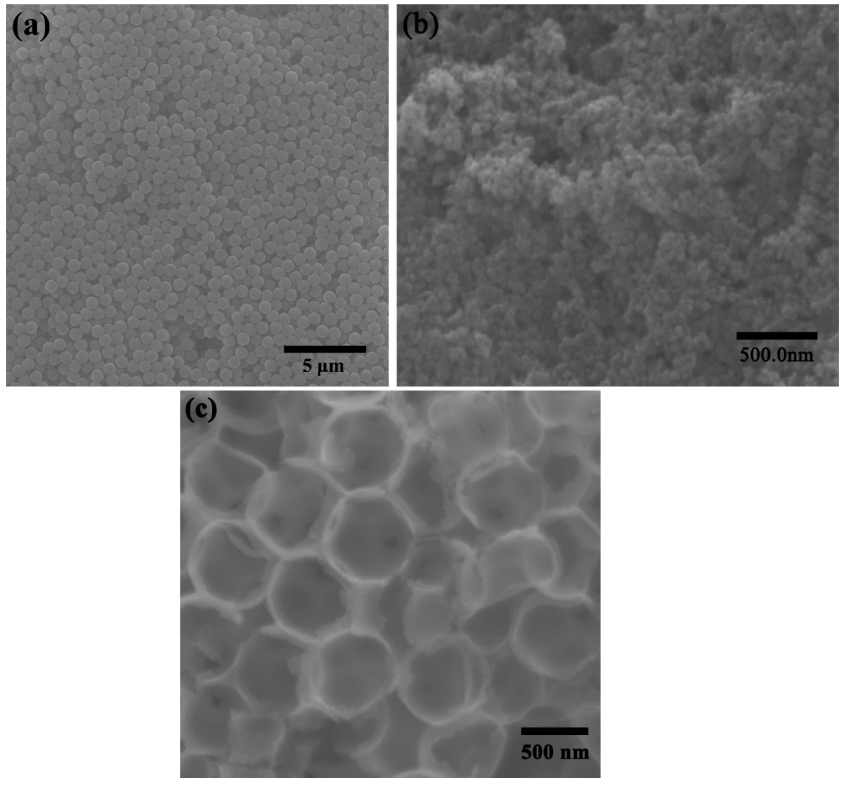

Figure 2. FE-SEM images of (a) 750 nm PS sphere, (b) SnO_2 nanoparticles, and (c) macroporous SnO_2.

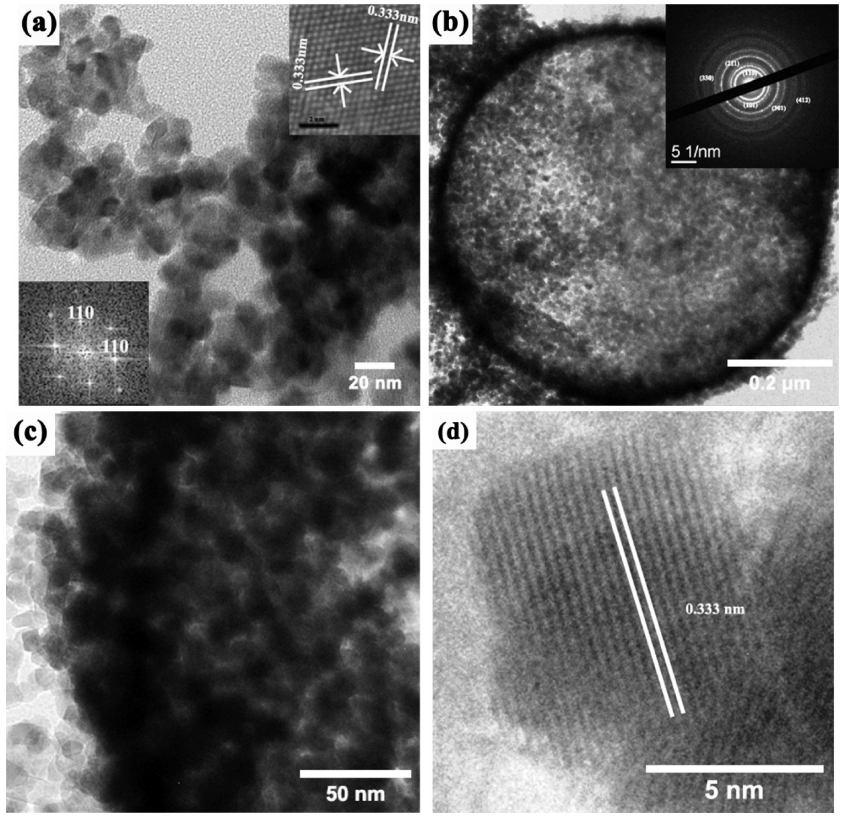

Figure 3. TEM, HR-TEM, and SAED images of (a) SnO_2 nanoparticles (FFT image is derived from the HR-TEM image) and (b–d) macroporous SnO_2 prepared at 500 °C for 1 h.

interesting to find that the SnO_2 nanocrystal-coated PS microsphere does not shrink much after the removal of PS sphere, which is about 20% of the size. That is significantly different from the 30–50% reduction in size for the

dx.doi.org/10.1021/am4009727 | ACS Appl. Mater. Interfaces 2013, 5, 5105–5111

macroporous TiO_2 prepared via sol−gel process, which can be attributed to the destruction of PS microsphere during the calcination process.[41]

Transmission electron microscopy (TEM) was carried out for a further discernment of SnO_2 nanoparticles and macroporous SnO_2. Figure 3a is a typical TEM image of SnO_2 nanocrystalline, which is ∼10 nm in diameter. The SnO_2 nanocrystal exhibits lattice fringers with a *d*-spacing of 0.333 nm that can be indexed as (110) plane, as shown in the HR-TEM image (inset in Figure 3a, right upper). Moreover, the corresponding Fast Fourier Transform (FFT) image (inset in Figure 3a, left lower) is derived from a single SnO_2 nanoparticle which combine with the HR-TEM image (inset of Figure 3a) can confirm the single-crystalline form of SnO_2 nanocrystal. The TEM image of macroporous SnO_2 indicates a pore diameter of about 650 nm (Figure 3b), which is similar to that obtained from the FE-SEM images (Figure 2c, d). Careful observation shows that the macroporous structure possess a darker ring, which is accumulated by the small SnO_2 nanoparticles with an average diameter of 10 nm obtained by statistics (Figure 3c). The result is coincident with the SnO_2 nanoparticles implying the PS microsphere made no influence on the size of NP-SnO_2 during the reflux process. The SAED image (Figure 3b, inset) reveals the multicrystalline structure of macroporous SnO_2. The HRTEM image of macroporous SnO_2 shows a *d*-spacing of 0.333 nm of single nanoparticle (Figure 3d), which can be indexed as (110) plane, confirming the same characteristics compared to as-synthesized SnO_2 nanoparticles.

The present SnO_2 nanoparticle and macroporous structure are used as photoanode for DSSCs applications. The current density−voltage (*J*−*V*) curves of the DSSCs based on NP-SnO_2 and macro-SnO_2 are shown in Figure 4a. Table 1 shows the

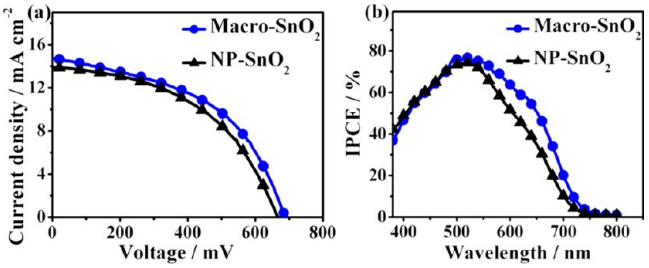

Figure 4. (a) *J*−*V* curves of DSSCs based on NP-SnO_2 (15 μm NP-SnO_2) and macro-SnO_2 (15 μm macro-SnO_2) photoanodes. (b) Incident-photon-to-current conversion efficiency (IPCE) spectra of DSSCs based on SnO_2.

Table 1. Short-Circuit Photocurrent Density (J_{sc}), Open-Circuit Voltage (V_{oc}), Fill Factor (FF), and Conversion Efficiency (η) for NP-SnO_2 and Macro-SnO_2-Based DSSCs

cell	J_{sc} (mA cm^{-2})	V_{oc} (mV)	FF	η (%)	adsorbed dye ($\times 10^{-8}$ mol cm^{-2}
NP-SnO_2	13.95	670	0.488	4.41	19.24
macro-SnO_2	14.74	690	0.490	4.87	14.00

photovoltaic parameters of two kinds of cells investigated in this article, the short-circuit current density (J_{sc}) and open circuit voltage (V_{oc}) are enhanced from 13.95 mA cm^{-2} for NP-SnO_2 to 14.74 mA cm^{-2} for macro-SnO_2 and 670 mV for NP-SnO_2 to 690 mV for macro-SnO_2, respectively. Because their fill factors are almost the same (∼0.49), the overall conversion efficiency (η) of NP-SnO_2 (4.41%) is lower than that of macro-SnO_2 (4.87%). In addition, the influences of $TiCl_4$ treatment on the photovoltaic parameters are further investigated. For example, the DSSC based on NP-SnO_2 photoelectrode without $TiCl_4$ treatment shows the J_{sc}, V_{oc}, and η are 10.35 mA cm^{-2}, 642 mV, and 2.78%, which are significantly inferior to the corresponding photovoltaic parameters of $TiCl_4$ treated NP-SnO_2 photoelectrode. This can be probably ascribed to the less defects after $TiCl_4$ treatment (a TiO_2 layer coats on the SnO_2 surface), which enabling better electron transfer from the TiO_2 to the SnO_2 and also avoid any extra internal trap sites.[42] Moreover, recent researches for both liquid and solid-state solar cells based on SnO_2 photoelectrode also supported the present results.[43]

The incident-photon-to-current efficiency (IPCE) spectra shown in Figure 4b are used as the function of wavelength (400−800 nm). Though the maximum value of IPCE spectra at around 530 nm (N719 absorption) is similar for the Marco-SnO_2 or NP-SnO_2 based DSSCs, the IPCE values of the former are significantly larger than that of the latter for the long wavelength region (530−750 nm) which can be attributed to the superior light scattering ability of the macro-SnO_2. The larger IPCE value of the DSSC based on macro-SnO_2 contributes to the higher J_{sc} compared to the NP-SnO_2, which is agreement with the *J*−*V* results. Besides, some previous reports of ZnO based DSSCs has the similar result. The DSSCs based on ZnO hollow sphere has shown an enhancement in J_{sc} compared to the ZnO nanoparticle which can be ascribed to the superior light scattering ability for the former.[13]

It is well-known that the J_{sc} depends on the charge harvesting efficiency (η_{lh}), charge-injection efficiency (η_{inj}) and the charge-collection efficiency (η_{cc}) according to eq 1:[44]

$$J_{sc} = q\eta_{lh}\eta_{inj}\eta_{cc}I_0 \quad (1)$$

(q is the elementary charge, I_0 is light flux). Here, the η_{inj} are assumed to the same for the two DSSCs because of the same dye (N719) adsorbed on the same semiconductor material (SnO_2).The η_{lh} relates to the dye loading and light scattering ability. The dye loading obtained from the UV−vis absorption measurement of the detached dye solution shows the NP-SnO_2 photoanode (13.89×10^{-8} mol cm^{-2}) has larger value than that of macro-SnO_2 (11.69×10^{-8} mol cm^{-2}) photoanode. This is reasonable since the nanoparticles possess a larger surface area compared with macroporous structure when the thicknesses are same. Hence, the less dye loading for the macro-SnO_2 exhibits larger J_{sc}, which must be ascribed to other factors, e.g., larger light scattering, faster electron transport, or lower recombination.

The light scattering ability of photoanode material is usually characterized by the UV−vis reflectance spectrum. Figure 5 shows the UV−vis reflectance spectra of NP-SnO_2 and macro-SnO_2 films without dye adsorption. Obviously, macro-SnO_2 film has higher reflectance than the NP-SnO_2 film in the wavelength range of 400−800 nm, indicating that the former has a better light scattering ability and the incident light is significantly scattered within the film of the former because of the comparable pore size to the wavelength of visible light. It increases the probability of light absorption by the sensitizers for the macro-SnO_2 film which will contribute to the enhancement of the J_{sc}.

In addition to the light harvesting efficiency, the charge collection efficiency (η_{cc}) also influences the J_{sc} according to the

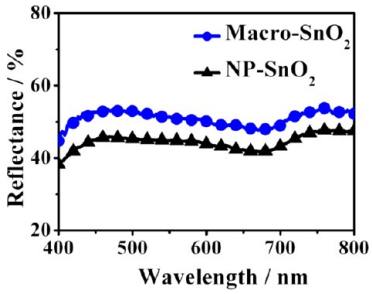

Figure 5. Diffuse reflectance spectra of NP-SnO_2 and macro-SnO_2 films.

above eq 1. The η_{cc} can be derived from the Intensity-modulated photocurrent spectroscopy (IMPS) and intensity-modulated photovoltage spectroscopy (IMVS) results through the following expression[45]

$$\eta_{cc} = 1 - \tau_d/\tau_r \quad (2)$$

The τ_d (τ_r) is the transport time (recombination time) which can be obtained from the expression $\tau_d = 1/2\pi f_d$ ($\tau_r = 1/2\pi f_r$), where f_d (f_r) is the characteristic frequency minimum of the IMPS (IMVS) imaginary component. Time constants of electron transport (IMPS) and electron recombination time (IMVS) as a function of light intensity are shown in Figure 6a,

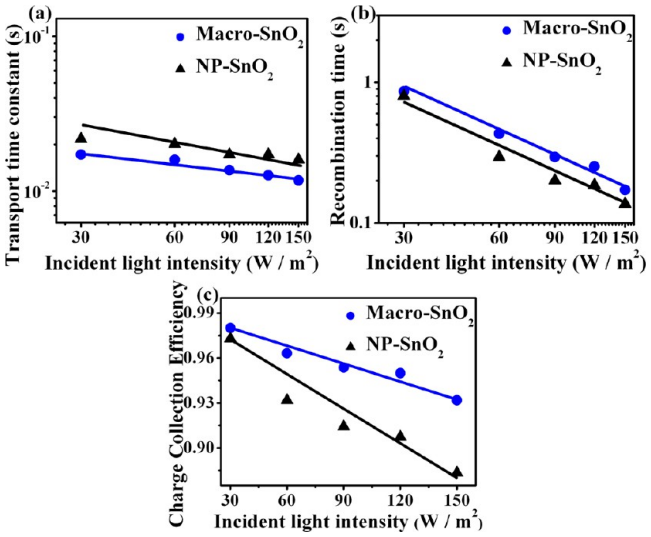

Figure 6. Incident light intensity dependent (a) electron transport time and (b) electron lifetime for SnO_2-DSSCs, all measurements were carried out at 457 nm LED illumination; (c) charge collection efficiency vs light intensity.

b. From the two figures we can see that the τ_d and τ_r decrease with increased light intensity. Thus, deep traps will be filled and electron trapping/detrapping involves shallower levels result in faster electron transport under circumstance with higher light intensities. In addition, the electron transport rate of the macro-SnO_2 based DSSC is faster than that of NP-SnO_2 at various light intensities (Figure 6a), which can be attributed to the less surface traps for the macro-SnO_2 because of its smaller surface area compared with the NP-SnO_2. The lower recombination time (τ_r) or lower electron lifetime for the NP-SnO_2 compared to the macro-SnO_2 (Figure 6b) is ascribed to the lager surface area that have more recombination sites and leading to a severe electron recombination. Hence the V_{oc} of DSSCs based on macro-SnO_2 is higher than that of NP-SnO_2.

On the basis of Figure 6a, b and eq 2, the charge collection efficiency vs light intensity of the two cells can be drawn in Figure 6c, which shows the macro-SnO_2-based DSSC has significantly higher η_{cc} than that of NP-based DSSC. This will help to improve the J_{sc}. According to the results and discussions above, the superior light scattering, faster electron transport and slower electron recombination finally result in the larger J_{sc} and higher V_{oc}; however, the fill factors of the two cells are similar (0.490 for macro-SnO_2 and 0.488 for NP-SnO_2) because of their same electrolyte and counter electrode. Finally, the power conversion efficiency of the DSSCs based on macro-SnO_2 photoelectrode (4.87%) is higher than that of NP-SnO_2 (4.41%).

The open circuit voltages (V_{oc}) of the DSSCs based on macro-SnO_2 and NP-SnO_2 are 690 and 670 mV, respectively. The V_{oc} variation of the two cells is further characterized by the electrochemical impedance spectroscopy (EIS). The Nyquist plots (Figure 7) of the two cells show two semicircles, where

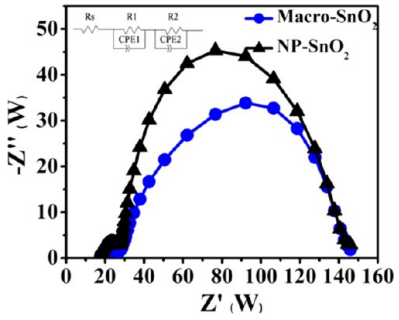

Figure 7. Electrochemical impedance spectra of NP-SnO_2 and macro-SnO_2 based DSSCs measured in dark and at a −0.7 V bias.

the smaller semicircles in high frequency range from 1 kHz to 1 MHz reflect the charge transfer at the counter electrode/electrolyte interface. Although the larger semicircles in low frequency range (0.1−1 kHz) correspond to the SnO_2/dye/redox (I^-/I_3^-) electrolyte interface. After analyzing the curves with a Z-view software by using an equivalent circuit (Figure 7, inset), the charge transfer resistance (R_1) of the two cells are similar because the same electrolyte and counter electrode were used which lead to similar fill factors. The charge recombination resistance (R_2, obtained from Z-view software) at the SnO_2/dye/electrolyte of the macro-SnO_2 and NP-SnO_2-based DSSCs are 77.87 and 114.9 Ω, respectively. The electron lifetimes by Z-view with expression: τ = CPE-T × R, where τ represents the lifetime and CPE-T represents the chemical capacitance. Although a larger R_2 for NP-SnO_2 structure, the electron lifetime of macro-SnO_2 (148 ms) is larger than that of NP-SnO_2 (129 ms), which is because of larger chemical capacitance for the macroporous SnO_2 structure. The longer electron lifetime for the macro-SnO_2 is in agreement with the IMVS data and also further supports its higher V_{oc} (see Figures 4a and 6b).

To explore the advantages of larger surface area of NP-SnO_2 and excellent light scattering ability, faster electron transport, and slower electron recombination of macro-SnO_2, we have designed a double-layered photoelectrode containing NP-SnO_2 (15.0 μm in thick) and macro-SnO_2 (5.0 μm in thick)for the DSSC. Figure 8 is the $J-V$ curve of the DSSC based on the

dx.doi.org/10.1021/am4009727 | ACS Appl. Mater. Interfaces 2013, 5, 5105−5111

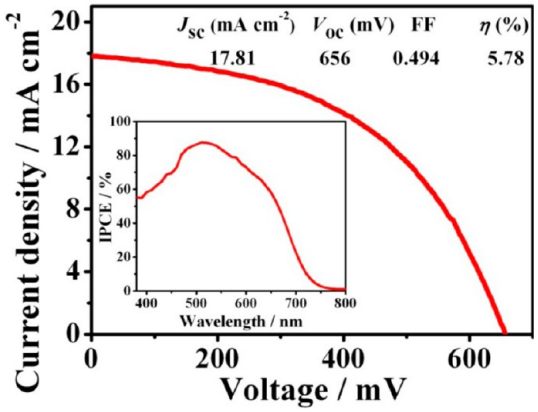

Figure 8. Photovoltaic performance of double layer-SnO_2 DSSC (15 μm NP-SnO_2 + 5 μm macro-SnO_2).

double-layer SnO_2 film showing significant power conversion efficiency (5.78%) with a J_{sc} value of 17.81 mA cm^{-2}, V_{oc} of 656 mV, and FF of 0.494. The IPCE (inset in Figure 8) also shows a much higher value than that of NP-SnO_2. The enhancement of J_{sc} from 13.87 mA cm^{-2} (NP-SnO_2) to 17.81 mA cm^{-2} (NP-SnO_2+macro-SnO_2) can be mainly ascribed to the higher dye loading and light scattering ability for the double-layer photoelectrode. For comparison, the NP-SnO_2 and macro-SnO_2 films with 20.0 μm in thickness were also prepared for DSSCs. The power conversion efficiency of double layered photoelectrode (5.78%) is larger than those of macro-SnO_2 (4.70%, 20.0 μm in thickness) or NP-SnO_2 (4.12%, 20.0 μm in thickness). One can see with the increase in the film thickness of the NP-SnO_2 or macro-SnO_2, the photovoltaic performance has a little drop compared to the 15 μm thick films because of serious electron recombination.

CONCLUSION

A simple reflux process has been developed to synthesize nanocrystalline and macroporous SnO_2. Though the lower dye loading for the macro-SnO_2 photoanode ascribing from the lower roughness factor, the power conversion of DSSC based on macro-SnO_2 (4.87%) was higher than that of NP-SnO_2 (4.41%) because of the superior light scattering ability, faster electron transport, and slower electron recombination which were confirmed by the UV−vis diffuse reflectance spectroscopy, IMPS, IMVS and EIS characterizations. Furthermore, the DSSC based on double-layer SnO_2 photoelectrode (15.0 μm NP-SnO_2+5.0 μm macro-SnO_2) exhibits an impressive power conversion of 5.78% with an enhancement of 31% compared to the single 15 μm NP-SnO_2 photoelectrode (4.41%) due to the higher dye loading and superior light scattering ability for the former. The macroporous SnO_2 structure may provide a new opportunity for the Li-ion battery, supercapacitor, solid-state electrolyte-based dye-sensitized solar cells or quantum dot-sensitized solar cells.

AUTHOR INFORMATION

Corresponding Author

*E-mail: kuangdb@mail.sysu.edu.cn.

Notes

The authors declare no competing financial interest.

ACKNOWLEDGMENTS

The authors acknowledge the financial supports from the Program for New Century Excellent Talents in University (NCET-11-0533), the Fundamental Research Funds for the Central Universities, and the Research Fund for the Doctoral Program of Higher Education (20100171110014), and Sun Yat-sen Innovative Talents Cultivation Program for Doctoral Graduate Student.

REFERENCES

(1) Frank, A. J.; Kopidakis, N.; Lagemaat, J. V. D. *Coord. Chem. Rev.* **2004**, *248*, 1165−1179.
(2) Durrant, J. R.; Haque, S. A.; Palomares, E. *Coord. Chem. Rev.* **2004**, *248*, 1247−1257.
(3) Wang, F. L.; Subbaiyan, N. K.; Wang, Q.; Rochford, C.; Xu, G. W.; Lu, R. T.; Elliot, A.; D'Souza, F.; Hui, R. Q.; Wu, J. *ACS Appl. Mater. Interfaces* **2012**, *4*, 1565−1572.
(4) Robertson, N. *Angew. Chem., Int. Ed.* **2006**, *45*, 2338−2345.
(5) Iglesias, M. G.; Pellejà, L.; Yum, J. H.; Rodríguez, D. G.; Nazeeruddin, M. K.; Grätzel, M.; Clifford, J. N.; Palomares, E.; Vázquez, P.; Torres, T. *Chem. Sci.* **2012**, *3*, 1177−1184.
(6) Gregg, B. A. *Coord. Chem. Rev.* **2004**, *248*, 1215−1224.
(7) Nogueira, A. F.; Longo, C.; De Paoli, M.-A. *Coord. Chem. Rev.* **2004**, *248*, 1455−1468.
(8) Kloke, A.; von Stetten, F.; Zengerle, R.; Kerzenmacher, S. *Adv. Mater.* **2011**, *23*, 4976−5008.
(9) O' Regan, B.; Grätzel, M. *Nature* **1991**, *353*, 737−740.
(10) Yella, A.; Lee, H. W.; Taso, H. N.; Yi, C.; Chandiran, A. K.; Nazeeruddin, M. K.; Diau, E. W. G.; Yeh, C. Y.; Zakeeruddin, S. M.; Grätzel, M. *Science* **2011**, *334*, 629−634.
(11) Sauvage, F.; Di Fonzo, F.; Bassi, A. L.; Casari, C. S.; Russo, V.; Divitini, G.; Ducati, C.; Bottani, C. E.; Comte, P.; Grätzel, M. *Nano Lett.* **2010**, *10*, 2562−2567.
(12) Zheng, Q.; Kang, H.; Yun, J. J.; Lee, J. Y.; Park, J. H.; Baik, S. *ACS Nano* **2011**, *6*, 5088−5093.
(13) Buonsanti, R.; Carlion, E.; Giannini, C.; Altamura, D.; Marco, L. D.; Giannuzzi, R.; Manca, M.; Gigli, G.; Cozzoli, P. D. *J. Am. Chem. Soc.* **2011**, *133*, 19216−19239.
(14) Hwang, D.; Kim, D. Y.; Jang, S. −Y.; Kim, D. *J. Mater. Chem. A* **2013**, *1*, 1228−1238.
(15) Chen, H. Y.; Kuang, D. B.; Su, C. Y. *J. Mater. Chem.* **2012**, *22*, 15475−15489.
(16) Liao, J. Y.; Lei, B. X.; Chen, H. Y.; Kuang, D. B.; Su, C. Y. *Energy Environ. Sci.* **2012**, *5*, 5750−5757.
(17) Wang, Y. F.; Li, J. W.; Hou, Y. F.; Yu, X. Y.; Su, C. Y.; Kuang, D. B. *Chem.—Eur. J.* **2010**, *16*, 8620−8625.
(18) Wang, Y. F.; Li, K. N.; Liang, C. L.; Hou, Y. F.; Su, C. Y.; Kuang, D. B. *J. Mater. Chem.* **2012**, *22*, 21495−21501.
(19) Shang, G.; Wu, J.; Tang, S.; Huang, M.; Lan, Z.; Li, Y.; Zhao, J.; Zhang, X. *J. Mater. Chem.* **2012**, *22*, 25335−25339.
(20) Teddy, Z.; Uddin, T.; Nicolas, Y.; Olivier, C.; Toupance, T.; Labrugère, C.; Hirsch, L. *ACS Appl. Mater. Interfaces* **2011**, *3*, 1485−1491.
(21) Magne, C.; Moehl, T.; Urien, M.; Grätzel, M.; Pauporté, T. *J. Mater. Chem. A* **2013**, *1*, 2079−2088.
(22) Zhang, Q. F.; Chou, T. P.; Russo, B.; Jenekhe, S. A.; Cao, G. Z. *Angew. Chem., Int. Ed.* **2008**, *47*, 2402−2406.
(23) Zhang, Q. F.; Chou, T. P.; Russo, B.; Jenekhe, S. A.; Cao, G. Z. *Adv. Mater.* **2008**, *18*, 1654−1660.
(24) He, C. X.; Lei, B. X.; Wang, Y. F.; Su, C. Y.; Fang, Y. P.; Kuang, D. B. *Chem.—Eur. J.* **2010**, *16*, 8757−8761.
(25) Dong, Z.; Lai, X.; Halpert, J. E.; Yang, N.; Yi, L.; Zhai, J.; Wang, D.; Tang, Z.; Jiang, L. *Adv. Mater.* **2012**, *24*, 1046−1049.
(26) Kim, D. W.; Shin, S. S.; Cho, I. S.; Lee, S.; Kim, D. H.; Lee, C. W.; Jung, H. S.; Hong, K. S. *Nanoscale* **2012**, *4*, 557−562.
(27) Zhang, Y. F.; Zhang, H.; Wang, Y. F.; Zhang, W. F. *J. Phys. Chem. C* **2008**, *112*, 8553−8557.

(28) Chen, J.; Lu, L.; Wang, W. *J. Phys. Chem. C* **2012**, *116*, 10841−10847.
(29) Li, Z.; Zhou, Y.; Bao, C.; Xue, G.; Zhang, J.; Liu, J.; Yu, T.; Zou, Z. *Nanoscale* **2012**, *4*, 3490−3494.
(30) Li, Y. F.; Wang, Y.; Chen, C. Y.; Pang, A. Y.; Wei, M. D. *Chem.—Eur. J.* **2012**, *18*, 11716−11722.
(31) Fukai, Y.; Kondo, Y.; Mori, S.; Suzuki, E. *Electrochem. Commun.* **2007**, *9*, 1439−1443.
(32) Zukalová, M.; Zukal, A.; Kavan, L.; Nazeeruddin, M. K.; Liska, P.; Grätzel, M. *Nano Lett.* **2005**, *5*, 1789−1792.
(33) Fonstad, C. G.; Rediker, R. H. *J. Appl. Phys.* **1971**, *42*, 2911−2918.
(34) Qian, J. F.; Liu, P.; Xiao, Y.; Jiang, Y.; Cao, Y. L.; Ai, X. P.; Yang, H. X. *Adv. Mater.* **2009**, *21*, 3663−3667.
(35) Wijeratne, K.; Akilavasan, J.; Thelakkat, M.; Bandara, J. *Electrochim. Acta* **2012**, *72*, 192−198.
(36) Cai, C. T.; Li, X. D.; Lu, B. G.; Chen, L. L.; Wang, Y. Q.; Teng, F.; Wang, J. T.; Zhang, Z. X.; Pan, X. J.; Xie, E. *Nanoscale* **2012**, *4*, 3475−3481.
(37) Gubbala, S.; Russell, H. B.; Shah, H.; Deb, B.; Jasinski, J.; Rypkema, H.; Sunkara, M. K. *Energy Environ. Sci.* **2009**, *2*, 1302−1309.
(38) Qian, J. F.; Liu, P.; Xiao, Y.; Jiang, Y.; Cao, Y. L.; Ai, X. P.; Yang, H. X. *Adv. Mater.* **2009**, *21*, 1−5.
(39) Tétreault, N.; Arsenault, É.; Heiniger, L.; Soheilnia, N.; Brillet, J.; Moehl, T.; Zakeeruddin, S.; Ozin, G. A.; Grätzel, M. *Nano Lett.* **2011**, *11*, 4579−4584.
(40) Goodwin, J. W.; Hearn, J.; Ho, C. C.; Ottewill, R. H. *Colloid Polymer Sci.* **1974**, *252*, 464−471.
(41) Zhao, J. Q.; Wan, P.; Xiang, J.; Tong, T.; Dong, L.; Gao, Z. N.; Shen, X. Y.; Tong, H. *Microporous Mesoporous Mater.* **2011**, *138*, 200−206.
(42) Snaith, H. J.; Ducati, C. *Nano lett.* **2010**, *10*, 1259−1265.
(43) Keys, A.; Grätzel, M. *Chem. Mater.* **2002**, *14*, 2930−2935.
(44) Zhu, K.; Neale, N. R.; Miedaner, A.; Frank, A. J. *Nano lett.* **2007**, *7*, 69−74.
(45) Schlichthörl, G.; Park, N. G.; Frank, A. J. *J. Phys. Chem. B* **1999**, *103*, 782−791.